# First-Principles Predictions of the Structure, Stability, and Photocatalytic Potential of Cu$_2$O Surfaces

Leah Isseroff Bendavid[†] and Emily A. Carter*[,‡]

Departments of [†]Chemical and Biological Engineering and [‡]Mechanical and Aerospace Engineering, Program in Applied and Computational Mathematics, and Andlinger Center for Energy and the Environment, Princeton University, Princeton, New Jersey 08544-5263, United States

ABSTRACT: For a photocatalytic reaction to be thermodynamically allowed, a semiconductor's band edges need to be placed appropriately relative to the reaction redox potentials. We apply a recently developed scheme for calculating band edges with density functional theory (DFT)-based methods to Cu$_2$O, evaluating its available thermodynamic overpotential for redox reactions such as water splitting and conversion of CO$_2$ to methanol. Because these calculations are surface dependent, we first study the low-index surfaces of Cu$_2$O using periodic DFT+U theory to characterize and identify the most stable surface, which will be the most catalytically relevant. We employ various techniques to calculate the surface energy,

including the method of "ab initio atomistic thermodynamics". The Cu$_2$O(111) surface with (1 × 1) periodicity and surface copper vacancies is identified as the most stable at all oxygen partial pressures, although the ideal stoichiometric Cu$_2$O(111) surface is relatively close in energy under oxygen-poor conditions. These surfaces are then used to calculate the band edges. Comparison of the band edges to redox potentials reveals that Cu$_2$O is thermodynamically capable of photocatalytic reduction of CO$_2$ to methanol and the reduction and oxidation of water.
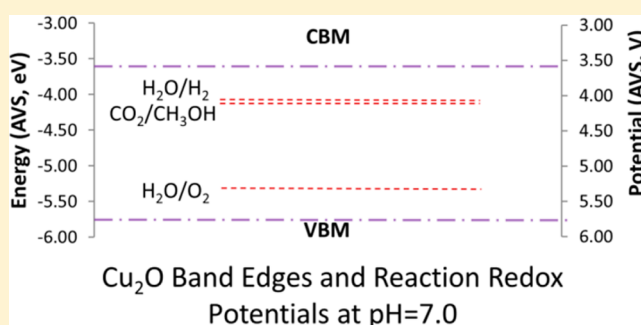
1. INTRODUCTION

For Cu$_2$O to be a functional photocatalyst for water splitting or the photoelectrosynthesis of, e.g., methanol from CO$_2$, catalysis of the redox reactions on its surface must first be thermodynamically favorable. This necessitates that the band edges bridge the reaction redox potentials; specifically, that the conduction band minimum (CBM) lies above the reduction reaction potential and that the valence band maximum (VBM) lies below the oxidation reaction potential

$$E_{CBM} > E_{red} \tag{1}$$

$$E_{VBM} < E_{ox} \tag{2}$$

Band edges can be determined from the onset of photocurrents in p-type Cu$_2$O, but this gives only approximate values because the sample is not ideal.[1] In situ electrochemical scanning tunneling microscopy (ECSTM) has also been used to directly observe the valence band edge, but these measurements are also affected by sample purity and morphology.[2] Consequently, a more accurate method of determining semiconductor band edges is needed to evaluate a material's thermodynamic capability for photocatalysis. The establishment of a robust method for calculating the band edges of Cu$_2$O will also aid further photocatalyst materials design when alloying with other compounds or constructing heterogeneous interfaces.

Density functional theory (DFT) provides a theoretical means of calculating band edges in an approach that builds on the first-principles calculation of a semiconductor's work function. The work function, ϕ, is defined as the energy required to move an electron from the Fermi level of a material to infinitely far away in a vacuum. This is equivalent to the energy difference between the vacuum level (E_{vac}) and the Fermi level (E_F), expressed as

$$\phi = E_{vac} - E_F \tag{3}$$

The Fermi energy can be calculated with Kohn−Sham (KS) DFT. However, within a periodic KS DFT calculation of bulk material, the Fermi energy and KS eigenvalues are not properly referenced to any absolute scale. This is because KS eigenvalues are arbitrarily shifted due to the use of pseudopotentials. It is therefore necessary to reference the KS eigenvalues to the vacuum energy within a single calculation. The reference is derived using a slab model, representing a semi-infinite surface with a vacuum region that eliminates interactions between periodic images, where the localized electrostatic potential in the vacuum region is defined as the reference vacuum level.

According to Janak's theorem, each occupied eigenvalue is given by the derivative of the total energy with respect to the occupation of its corresponding orbital.[3] This implies that the highest occupied eigenvalue, or the KS VBM (properly

referenced to the vacuum level), is exactly equal to the ionization potential of a material. Therefore, calculations of ϕ typically use the vacuum-referenced KS VBM as the reference point for the overall band structure.[4−7] The Fermi level in semiconductors is often defined as E_{VBM} in many electronic structure software packages, and so the ϕ obtained in this manner is an upper limit to the true value. The formal definition of the Fermi level in an undoped semiconductor is the energy halfway between the VBM and the CBM. Therefore, an alternative is to define $E_F = E_{VBM} + (1/2)E_g$, which can improve accuracy in some cases but also requires experimental knowledge of the band gap or an accurate method of obtaining it theoretically. It is difficult to obtain E_{CBM} directly from a single DFT calculation, as an exact relationship cannot be defined between the lowest unoccupied eigenvalue and the electron affinity because of the derivative discontinuity of the exchange-correlation (XC) potential.[8] Therefore, E_{CBM} is subsequently determined by adding an experimentally or theoretically derived fundamental band gap, E_g, to the E_{VBM} reference.

This approach of using E_{VBM} as a reference is problematic, in that both the KS E_{CBM} and E_{VBM} are systematically underestimated and overestimated, respectively, due to the missing derivative discontinuity in standard evaluations of the XC energy.[9] However, Perdew and Levy showed that the band gap center (BGC) can be predicted exactly using DFT.[8] Thus, a more accurate reference for band calculations is E_{BGC} instead of the conventional E_{VBM}, and E_{VBM} and E_{CBM} can be subsequently determined by subtracting or adding half of the fundamental band gap

$$E_{VBM} = E_{BGC} - \frac{1}{2}E_g \tag{4}$$

$$E_{CBM} = E_{BGC} + \frac{1}{2}E_g \tag{5}$$

The value of E_g must be computed from first principles for this approach to be free from empiricism. Because the eigenvalue gap from KS DFT does not directly correlate to the fundamental gap due to the derivative discontinuity, a higher level of theory must be used to calculate E_g. The fundamental gap can be derived using the GW approximation, a method within many-body perturbative Green's function theory, which can be used to calculate electronic quasiparticle excitations. We have previously shown that a "one-shot" GW approach (denoted G_0W_0) can accurately calculate the fundamental band gap of Cu_2O.[10]

This methodology for calculating band edges has been previously developed in the work by Toroker et al.[11] Other approaches to calculating band edges have been suggested, such as using GW directly with the slab model,[12,13] but the prohibitive expense of those calculations lends greater feasibility to our suggested approach. It is important to note that this model is approximate, as we consider only a clean, defect-free surface with no solvent present.

Because the work function is surface-dependent, we need to identify the most stable surface of Cu_2O, as it will be the predominant surface experimentally and will thus be the relevant surface for determining ϕ. This affords us the opportunity to develop a foundational understanding of the surfaces of Cu_2O. We focus on the low-index surfaces—the polar (100) and (110) surfaces and the nonpolar (111) surface. These have been previously experimentally[14,15] or theoret-

ically[16−20] characterized to some extent, and we defer a review of previously published work until the discussion of our results, where they will serve as a comparison. A better understanding of the surface properties of Cu_2O will lay essential groundwork for later studies of its surface chemistry. For this application, most essentially, our goal is to identify the most stable surface. Soon et al.[19,20] have previously characterized the low-energy surface structures using DFT with the Perdew−Burke−Ernzerhof (PBE) functional[21,22] and ab initio atomistic thermodynamics, which defines the surface energy as the difference between the total Gibbs free energy of the surface and the sum of the chemical potentials of its component atoms. Here, we begin by calculating the surface energy of these low index surfaces as the difference between total energies of the surface slabs and the bulk. For nonstoichiometric slabs, we use a variation of this approach to calculate a surface energy related to its cleavage plane. Finally, we calculate surface energies according to the ab initio atomistic thermodynamic approach and compare the results to the surface energies defined using the previous method. Our study differs from that of Soon et al. in that we mostly restrict the surface terminations and reconstruction periodicities that we consider to those that have been previously experimentally identified in single-crystal Cu_2O. Additionally, we use a different DFT approach, as we employ the DFT+U method.[23,24]

The main goals of this body of work are twofold: (1) to elucidate the surface structures and surface energies of Cu_2O and (2) to develop a framework of determining its band edges. We begin by characterizing the low-index surfaces of Cu_2O with a number of different surface terminations and reconstruction periodicities, to better understand the surface properties of its various faces. We then calculate the energies of these surfaces. Once we identify the most stable surface, that surface is used to derive the E_{BGC} reference, which, in combination with the G_0W_0-derived E_g,[10] is then used to calculate the band edge energies. We contrast this approach to the typical method of obtaining E_{VBM} by directly referencing the KS VBM to the vacuum level. As these calculations are dependent on the XC functional used and the level of exact exchange incorporated in the DFT-based approach, we determine the band edges using a variety of methods. Finally, the calculated band edges are compared to the redox potentials of the reactions of interest to evaluate photocatalytic capabilities.

2. COMPUTATIONAL METHODS

We model the structure and calculate the energies of the low-index surfaces—(100), (110), and (111). Only the (100) and (111) surfaces have been experimentally characterized, and we study the five different surface terminations that have been identified by Schulz and Cox.[14] For the (100) surface, there is the ideal O-terminated surface with (1×1) periodicity, the reconstructed Cu-terminated surface with $(3\sqrt{2} \times \sqrt{2})R45°$ periodicity, and the reconstructed surface with $(\sqrt{2} \times \sqrt{2})R45°$ periodicity and 1/2 of a terminating oxygen monolayer. For the (111) surface, there is the ideal O-terminated surface with (1×1) periodicity and the reconstructed surface with $(\sqrt{3} \times \sqrt{3})R30°$ periodicity and 2/3 of a terminating oxygen monolayer. However, for each of the (111) surfaces, there are two theoretical models that are in agreement with low-energy electron diffraction and scanning tunneling microscopy data.[15] The first model is where the ideal (1×1) surface is bulk terminated and the reconstructed $(\sqrt{3} \times \sqrt{3})R30°$ surface only differs by its ordered oxygen

vacancies. The second model is the same as the first, except that the coordinatively unsaturated copper ions in the surface copper layer are missing in both the ideal and reconstructed surfaces (henceforth denoted the (1×1)-V_{CuCUS} and $(\sqrt{3} \times \sqrt{3})R30°$-$V_{CuCUS}$ surfaces). We consider both of these models in our study. Because the (110) surface has not been experimentally characterized, we study (110) surface terminations of both copper and mixed copper/oxygen with (1×1) periodicity.

Ideally, the Heyd–Scuseria–Ernzerhof (HSE) hybrid XC functional[25−27] should be used to construct the initial geometries for slabs, to relax structures, and to calculate surface energies, as the HSE functional was shown to be most accurate in calculating the ground state properties of Cu_2O.[10] However, because of the expense of the hybrid functional and the size of some of the larger slabs, the DFT+U method[23,24] with PBE (denoted henceforth as PBE+U) was used to generate and optimize structures and calculate surface energies, as it benefits from decreased computational expense while maintaining accuracy in calculating bulk geometries (for a U−J of 6 eV).[10] The equilibrium bulk unit cell lattice parameters as derived by HSE and PBE+U differ by only 0.015 Å, so the effect of the functional choice on the initial structures will be minimal. The surface vectors for the (1×1) (111) surface were $u = v = 6.044$ Å with an angle of 120° between them; for the reconstructed (111) surface, $u = v = 10.469$ Å with an angle of 60°; for the ideal (100) surface, u and v are orthogonal and equal to 4.274 Å; for the reconstructed $(\sqrt{2} \times \sqrt{2})R45°$ (100) surface, u and v are orthogonal and equal to 6.044 Å; for the reconstructed $(3\sqrt{2} \times \sqrt{2})R45°$ (100) surface, u and v are orthogonal with $u = 18.132$ Å and $v = 6.044$ Å; for the ideal (110) surface, the lattice vectors are orthogonal, with $u = 4.274$ Å and $v = 6.044$ Å. After initial construction from the bulk structure, all ionic positions in the slab were allowed to relax using the PBE+U functional with a U−J of 6 eV, to observe the nature of reconstruction and study the extent of the relaxation in the equilibrium structure.

The surface energy, γ, can be obtained from a slab containing two identical surfaces, via the equation

$$\gamma = \frac{1}{2A}\left(E_{slab} - \frac{N_s}{N_b}E_{bulk}\right) \tag{6}$$

where E_{slab} is the total energy of a stoichiometric slab, E_{bulk} is the total energy of a bulk formula unit, N_s is the number of atoms in the slab, N_b is the number of atoms in the bulk formula unit, A is the unit surface area, and the factor $1/2$ is used because the slab has two surfaces. This formula can be applied to surfaces in stoichiometric slabs, but those that are in nonstoichiometric slabs do not have a defined surface energy according to this equation. We propose an alternative method to calculate an estimate of the surface energies for cleavage planes that cannot be modeled with stoichiometric slabs, using an average of two separate calculations with nonstoichiometric slabs whose sum atomic composition (scaled per surface area) would be a stoichiometric ratio. The approximate surface energy is defined as

$$\gamma_{avg} = \frac{1}{2}\left[\frac{1}{2A_1}\left(E_{slab,1} - \frac{N_{s,1}}{N_b}E_{bulk}\right) + \frac{1}{2A_2}\right.$$
$$\left.\left(E_{slab,2} - \frac{N_{s,2}}{N_b}E_{bulk}\right)\right] \tag{7}$$

where all variables are defined similarly to eq 6, but the subscripts 1 and 2 refer to the two nonstoichiometric slabs with different surface terminations. This model is only valid if $(N_{s,1}/A_1) + (N_{s,2}/A_2)$ results in a stoichiometric ratio of atoms, and therefore, the appropriate surface terminations must be chosen to balance the surface nonstoichiometry.

Alternatively, the surface energy in both stoichiometric and nonstoichiometric slabs can also be defined according to ab initio atomistic thermodynamics,[28,29] which takes into account the impact of a surrounding gas-phase environment on surface stability. Atomistic thermodynamics considers the surface in equilibrium with an environmental reservoir of oxygen whose temperature T and pressure p are variable. Within this approach, the surface energy of the slab model is defined as

$$\gamma(T, p) = \frac{1}{2A}[G_{slab}(T, p, N_{Cu}, N_O) - N_{Cu}\mu_{Cu}(T, p)$$
$$- N_O\mu_O(T, p)] \tag{8}$$

where G_{slab} is the total Gibbs free energy of the slab, N_{Cu} and N_O are the numbers of atoms of copper and oxygen in the slab, respectively, and μ_{Cu} and μ_O are the chemical potentials of copper and oxygen, respectively. The thermodynamic reservoir is constrained by the equilibrium of the chemical potentials with the Gibbs free energy of the bulk oxide

$$2\mu_{Cu}(T, p) + \mu_O(T, p) = g^{bulk}_{Cu_2O}(T, p) \tag{9}$$

where $g^{bulk}_{Cu_2O}$ is the Gibbs free energy of the bulk per formula unit. At O-poor conditions (i.e., low chemical potential of oxygen), all oxygen would leave the sample, and the sample would decompose into copper metal and oxygen gas. This defines an upper bound to the chemical potential of copper, with its maximum defined as

$$\max[\mu_{Cu}(T, p)] = g^{bulk}_{Cu}(T, p) \tag{10}$$

where g^{bulk}_{Cu} is the Gibbs free energy of bulk copper per atom. Similarly, we can define an upper bound to the oxygen chemical as when gas-phase oxygen would condense on the oxide surface. We can estimate this upper limit to the chemical potential as half of the energy of an isolated O_2 molecule at 0 K

$$\max[\mu_O(T, p)] = \frac{1}{2}E_{O_2} \tag{11}$$

Equations 10 and 11 can each be used in conjunction with eq 9 to derive the complementary chemical potential of the other atomic species.

We can significantly simplify eq 8 to derive an expression for the surface energy at both the upper and lower bounds of the oxygen chemical potential. To begin with, we can assume that the contributions of pV terms and zero-point energies of the solids contribute negligibly to the surface energy,[28,29] and so Gibbs free energies in eqs 8−10 can be approximated by total energies extracted from DFT calculations. In the O-poor limit, eq 10 fixes the copper chemical potential at its maximum

C

dx.doi.org/10.1021/jp406454c | J. Phys. Chem. B XXXX, XXX, XXX−XXX

$$\mu_{Cu}(T, p) = E_{Cu}^{bulk} \tag{12}$$

and eq 9 can then be used to define the oxygen chemical potential as

$$\mu_{O}(T, p) = E_{bulk} - 2E_{Cu}^{bulk} \tag{13}$$

where E_{bulk} is the total energy per formula unit of bulk Cu_2O. Therefore, in the O-poor limit, eq 8 simplifies to

$$\gamma_{O\text{-poor}} \approx \frac{1}{2A}[E_{slab} - N_O E_{bulk} - (N_{Cu} - 2N_O)E_{Cu}^{bulk}] \tag{14}$$

This equation is valuable in that it involves only slab or bulk quantities and avoids the more challenging calculation of molecular energies. Alternatively, in the O-rich limit, eq 11 fixes the maximum of the oxygen chemical potential as

$$\mu_{O}(T, p) = \frac{1}{2}E_{O_2} \tag{15}$$

and eq 9 can then be used to define the copper chemical potential as

$$\mu_{Cu} = \frac{1}{2}\left(E_{bulk} - \frac{1}{2}E_{O_2}\right) \tag{16}$$

In the O-rich limit, eq 8 simplifies to

$$\gamma_{O\text{-rich}} \approx \frac{1}{2A}\left[E_{slab} - \frac{N_{Cu}}{2}E_{bulk} - \frac{1}{2}\left(N_O - \frac{N_{Cu}}{2}\right)E_{O_2}\right] \tag{17}$$

The surface energy between these two extremes depends linearly on the oxygen chemical potential. Equations 14 and 17 are both equivalent to eq 6 for stoichiometric slabs, so the two methods of calculating surface energies only differ for nonstoichiometric slabs.

E_{Cu}^{bulk} was calculated using the four-atom fcc bulk copper unit cell with a Γ-point-centered $16 \times 16 \times 16$ k-point mesh (2052 irreducible k-points), which converged the total energy to within 1 meV/atom. For consistency with Cu_2O calculations, all calculations on bulk copper used PBE+U with $U-J = 6$ eV. The equilibrium lattice constant of the optimized unit cell was 3.603 Å, in close agreement with 3.615 from experiment.[30] Our calculated E_{Cu}^{bulk} was -1.751 eV. E_{O_2} was calculated by modeling the $^3\Sigma_g^-$ ground state of an isolated O_2 molecule in an orthorhombic periodic cell with lattice vectors 9.0, 9.1, and 9.2 Å. (The DFT wave function is not a true triplet because open-shell spin-polarized DFT produces eigenfunctions of $\hat{S}_z$ but not $\hat{S}^2$.) This calculation used a planewave kinetic energy cutoff of 900 eV and integrated the Brillouin zone using Gaussian smearing with a smearing width of 0.0001 eV. The optimized bond length was 1.232 Å, close to the experimental bond length of 1.21 Å.[31] Our calculated E_{O_2} was -9.777 eV, which includes contributions from the zero-point energy.

We determined the number of layers needed to converge the surface energy (using eqs 6 and 7 for unreconstructed, structurally relaxed slabs), and these numbers of layers were used in calculations for both ideal and reconstructed surfaces. The surface energy was converged to within 10 mJ/m^2 for slabs containing five trilayers for the ideal bulk-terminated (111) surface (where each trilayer consists of a layer of four copper atoms sandwiched between two layers of one oxygen atom each, corresponding to a total of 30 atoms in the slab), 11 layers for the mixed Cu/O-terminated (110) surface (with two atoms per Cu layer, four atoms per mixed Cu/O layer, corresponding

to a total of 34 atoms in the slab), and 17 layers for the ideal O-terminated (100) surface (with two atoms per Cu layer and one atom per O layer, corresponding to a total of 25 atoms in the slab). Vacuum (13 Å) was used to separate slabs from their periodic images.

The Vienna Ab-Initio Simulation Package (VASP v. 5.2.2) was used for all DFT calculations,[32] with Blöchl's all-electron, frozen-core projector augmented wave (PAW) method used to represent the nuclei and core electrons ([He] core for O and [Ar] core for Cu).[33] PAW potentials were obtained from the VASP package, with the standard PAW potential for O. The formalism of Dudarev et al. was used for DFT+U.[34] A Γ-point-centered k-point mesh of $4 \times 4 \times 1$ was used for all (111) surfaces and the reconstructed $(\sqrt{2} \times \sqrt{2})R45°$ (100) surface. k-point meshes of $6 \times 6 \times 1$, $2 \times 4 \times 1$, and $6 \times 4 \times 1$ were used for the ideal (100), reconstructed $(3\sqrt{2} \times \sqrt{2})R45°$ (100), and ideal (110) surfaces, respectively. Brillouin zone integration employed Gaussian smearing with a smearing width of 0.01 eV for all structural optimizations, whereas final single-point energies were calculated using the tetrahedron method with Blöchl corrections.[35] The structures were optimized with a force convergence threshold of 0.03 eV Å^{-1}. All calculations used a planewave kinetic energy cutoff of 700 eV, which had converged the total energy of the bulk unit cell to within 1 meV/atom.

Calculation of the VBM and BGC was done on slabs with the (1×1) (111) surfaces (both surface models), which were identified as the lowest-energy surfaces under ultrahigh vacuum (vide infra). We used PBE+U, hybrid DFT with PBE0,[36] and HSE to calculate the electron density and band structure for the (111) surface in the periodic slab model. The local electrostatic potential was averaged in the x and y directions to obtain the potential along the z direction (perpendicular to the surface of the slab), including the potential in the vacuum region. Either the KS VBM was referenced directly to E_{vac} to determine E_{VBM} or E_{BGC} was taken to be halfway between E_{VBM} and E_{CBM} in the surface unit cell and referenced to E_{vac}.

For hybrid-DFT calculations with the HSE XC functional, 25% of PBE exchange is replaced by screened nonlocal exact exchange, and the recommended value of 0.2 Å^{-1} was used for the screening parameter.[37] The q-point mesh in the Hartree−Fock (HF) kernel calculation for PBE0 and HSE was not reduced.

3. RESULTS AND DISCUSSION

3.1. Cu$_2$O Surface Structures and Surface Energies.
The equilibrium structures of each of the low-index surfaces were characterized prior to calculating surface energies. For the (100) surface, we used slab models replicating the surfaces identified from experimental data. On the basis of low-energy electron diffraction patterns and X-ray photoelectron spectroscopy Cu-to-O ratios, Schulz and Cox proposed models of an O-terminated (1×1) surface, a reconstructed surface with $(\sqrt{2} \times \sqrt{2})R45°$ periodicity associated with a 1/2 terminating oxygen monolayer, and a reconstructed $(3\sqrt{2} \times \sqrt{2})R45°$ Cu-terminated surface.[14] They suggested that the reconstruction of the $(3\sqrt{2} \times \sqrt{2})R45°$ surface is a relaxation of singly coordinated surface copper cations, with surface dimer formation between adjacent cations in neighboring rows along the $[011]$ or $[01\bar{1}]$ directions in intervals of $(3/2)\sqrt{2}$. By oxygenating this surface, the 1/2 monolayer of oxygens disrupts the Cu^+-Cu^+ interactions, lifting the reconstruction and resulting in a new periodicity of $(\sqrt{2} \times \sqrt{2})R45°$. We
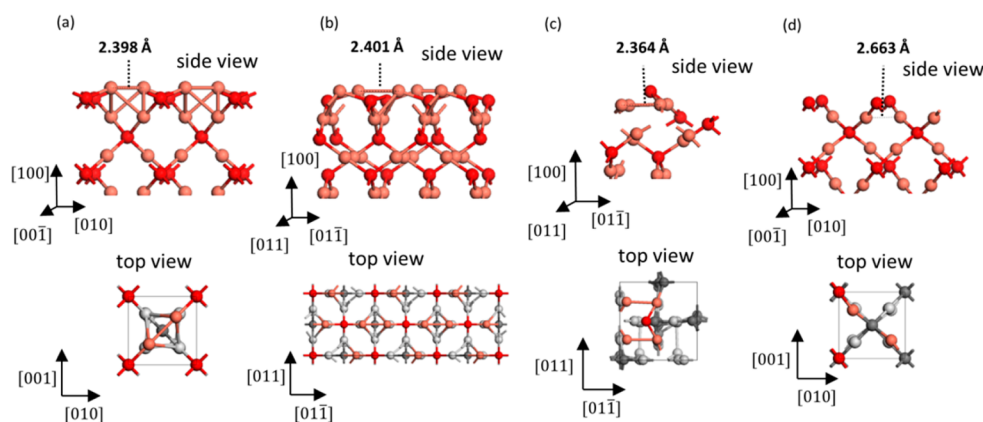
Figure 1. Relaxed geometries of the $Cu_2O(100)$ surface. Side and top views of (a) Cu-terminated (1×1) surface, (b) Cu-terminated $(3\sqrt{2} \times \sqrt{2})R45°$ surface, (c) 1/2 O-terminated $(\sqrt{2} \times \sqrt{2})R45°$ surface, and (d) O-terminated (1×1) surface. Red and pink spheres represent oxygen and copper atoms, respectively. The top view of surfaces represents subsurface layers in gray, where darker gray represents oxygen. Cu−Cu surface dimer bond lengths are labeled in the side views.

explore their interpretation of the surface structures in what follows.

Previous DFT-PBE and DFT-PW92 studies of a Cu-terminated (1×1) (100) surface predicted the formation of surface Cu−Cu dimers with a 2.374−2.403 Å bond distance significantly contracted from the bulk value of 3.016−3.053 Å, where the copper and oxygen ions at the surface are almost in the surface plane.[16,17,19] Our PBE+U model of the Cu-terminated (1×1) (100) surface resulted in a similar surface relaxation (Figure 1a), with a Cu−Cu distance contracted from 3.022 to 2.398 Å. However, the (1×1) model does not allow for surface dimers to form with the experimentally observed periodicity, so a slab with $(3\sqrt{2} \times \sqrt{2})R45°$ lattice vectors was used to model the reconstruction. When the larger $(3\sqrt{2} \times \sqrt{2})R45°$ model was fully relaxed (Figure 1b) from multiple initial structures, all of the surface copper atoms still formed surface dimers, with contracted Cu−Cu bond lengths of 2.393 Å. In additional conflict with the experimental interpretation, dimer formation was not restricted to between adjacent cations in neighboring rows along the $[011]$ or $[01\bar{1}]$ directions. Hence, this calculated structure is not in agreement with the experimental model of reconstruction. Molecular dynamics with simulated annealing may be needed to capture the true surface structure, as it is impossible to sample the full configuration space for the initial surface structures.[38] This approach has been used previously to explain the surface reconstruction of the Cu-terminated (100) surface.[39]

One challenge to the experimental model is in the theoretically predicted reconstruction of the relaxed $(\sqrt{2} \times \sqrt{2})R45°$ surface. While Schulz and Cox proposed that the surface oxygens prevent all surface copper dimer formation, lifting the reconstruction periodicity from $(3\sqrt{2} \times \sqrt{2})R45°$ to $(\sqrt{2} \times \sqrt{2})R45°$, our model predicts that surface dimers still form between copper atoms along the $[01\bar{1}]$ direction, with a dimer bond length of 2.364 Å (Figure 1c). Therefore, removal of Cu−Cu dimers cannot be used to explain the difference in reconstruction periodicities; rather, the surface oxygen atoms likely lift the reconstruction periodicity by restructuring the types of Cu−Cu dimers able to form on the surface.

Our model of the O-terminated (100) (1×1) surface showed no surface Cu−Cu dimer formation (Figure 1d). The surface Cu−O bonds also contracted slightly from 1.851 to

1.744 Å, in agreement with the surface relaxation observed in ref 19.

There was no experimental model to use for the (110) surface, as it has not been observed on single-crystal samples and therefore has not been experimentally characterized. We thus use only the ideal (1×1) periodicity with both possible terminations, pure copper and mixed Cu/O. The relaxed structure of the (110) surface has been investigated previously with DFT-PBE.[19] Relaxation of the (110) surface can best be described by the interlayer spacing between two consecutive CuO layers, $d_{CuO-CuO}$, or the Cu−Cu bond length between two successive Cu layers, d_{Cu-Cu}. The previous DFT study predicted a reduction of $d_{CuO-CuO}$ for the CuO-terminated surface but an expansion in $d_{CuO-CuO}$ for the Cu-terminated surface. In our model of the CuO-terminated surface, significant relaxation occurs, with a $d_{CuO-CuO}$ contraction from 3.022 to 2.738 Å (Figure 2a). For the Cu-terminated surface, $d_{CuO-CuO}$ increases only slightly by 0.059 Å, but there is substantial relaxation by the contraction of the surface d_{Cu-Cu} from 3.022 to 2.775 Å (Figure 2b). The overall trend in the (110) surface is therefore
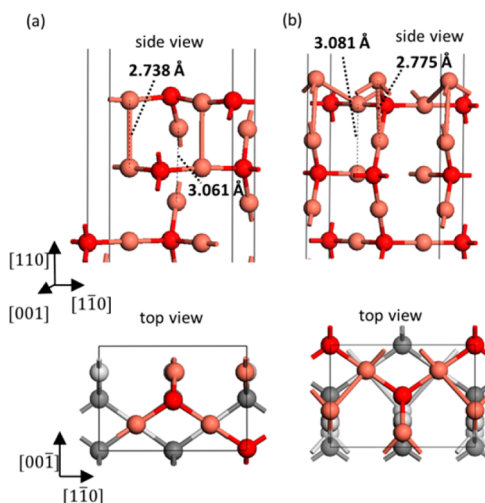

Figure 2. Relaxed geometries of the $Cu_2O(110)$ surface. Side and top views of (a) the Cu/O-terminated surface and (b) the Cu-terminated surface. Values for $d_{CuO-CuO}$ and d_{Cu-Cu} for the layers closest to the surface are labeled in the side views.
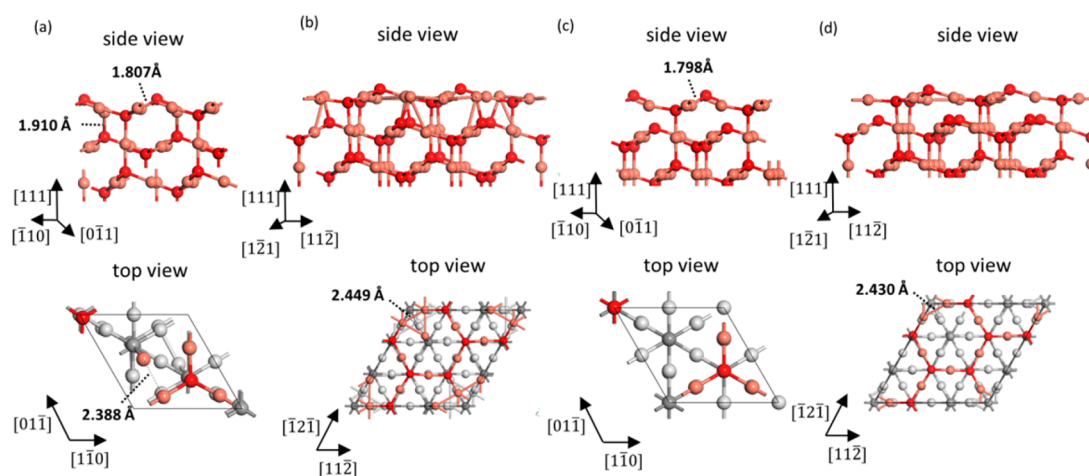
Figure 3. Relaxed geometries of the $Cu_2O(111)$ surface. Side and top views of (a) the O-terminated (1×1) surface, (b) the 2/3 O-terminated $(\sqrt{3} \times \sqrt{3})R30°$ surface, (c) the O-terminated (1×1)-V_{CuCUS} surface with surface copper vacancies, and (d) the 2/3 O-terminated $(\sqrt{3} \times \sqrt{3})R30°$-$V_{CuCUS}$ surface with surface copper vacancies.

Table 1. Bader Charges (e) of the $Cu_2O(111)$ Surfaces[a]

atom	(1×1)	$(\sqrt{3} \times \sqrt{3})R30°$	(1×1)-V_{CuCUS}	$(\sqrt{3} \times \sqrt{3})R30°$-$V_{CuCUS}$
$O_{CUS,1}$	−0.95	−0.99	−0.94	−0.95
$Cu_{CUS,1}$	0.37	0.37	−	−
$Cu_{NN,1}$	−	0.22	−	0.28
O_1	−1.00	−1.00	−1.02	−1.01
Cu_1	0.54	0.53	0.60	0.60
$O_{CUS,2}$	−	−	−0.96	−0.96
O_2	−1.00	−0.99	−0.97	−0.98
Cu_2	0.50	0.50	0.53	0.53
O_3	−1.00	−1.00	−1.02	−1.01
Cu_3	0.50	0.50	0.50	0.50
O_{bulk}			−1.01	
Cu_{bulk}			0.51	

[a]Bader charges are given for the coordinatively unsaturated surface oxygen atoms (O_{CUS}), the unsaturated surface copper atoms (Cu_{CUS}), the copper atoms made unsaturated by a surface oxygen vacancy (Cu_{NN}), and the saturated atoms (only numerically subscripted) in each trilayer. The numeral subscript gives the layer number, where 1 is the surface layer.

that the outermost surface, regardless of termination, contracts inward.

The (111) surface has been characterized by Schulz and Cox, who proposed the first models of the ideal stoichiometric O-terminated (1×1) surface and a reconstructed $(\sqrt{3} \times \sqrt{3})R30°$ surface with 1/3 monolayer of oxygen vacancies, where the coordinatively unsaturated copper atoms remain in the surface. In our study of these models, we first observed negligible relaxation of the ideal surface when beginning the optimization from the bulk-terminated surface, in overall agreement with previous DFT-PBE predictions.[18,19,40] However, calculation of the numerical Hessian revealed that this surface structure contains imaginary vibrational frequencies, indicating that the surface relaxed to a metastable state. (This was the surface used to calculate the band edges in the earlier work by Toroker et al.[11] and is the source of differences in their values.) To find the true stable minimum, we perturbed the surface atoms in the direction of the imaginary eigenvectors and relaxed the structure further. This broke the symmetry of the surface and resulted in the formation of surface copper dimers with bond lengths of 2.388 Å (Figure 3a). The surface bond between the linearly coordinated copper and the coordinatively unsaturated oxygen contracts slightly from the bulk length of 1.851 to 1.807 Å, while the bond between a subsurface oxygen

and the coordinatively unsaturated copper lengthens to 1.910 Å. The reconstructed $(\sqrt{3} \times \sqrt{3})R30°$ surface has a very different surface structure and charge density as a result of the oxygen vacancy. Figure 3b shows the relaxed surface structure of the $(\sqrt{3} \times \sqrt{3})R30°$ surface. The coordinatively unsaturated surface copper atoms have drifted toward the oxygen vacancy, creating a cluster of copper ions. Typical Cu−Cu distances in the bulk are 3.022 Å, while these surface copper atoms are separated by distances of 2.449 Å.

We also studied the structures of the second model for the ideal and reconstructed (111) surfaces, where the surfaces lack the coordinatively unsaturated copper atoms. The (1×1)-V_{CuCUS} surface showed negligible reorganization from the bulk-terminated structure (Figure 3c). Here, too, the surface bond between the linearly coordinated copper and the coordinatively unsaturated oxygen contracts from the bulk length of 1.851 to 1.798 Å. The unsaturated copper atoms in the $(\sqrt{3} \times \sqrt{3})R30°$-$V_{CuCUS}$ surface still drift toward the oxygen vacancy to create a cluster of cations, with a surface Cu−Cu bond length of 2.430 Å.

We used Bader analysis[41] to examine the electron density distribution of the (111) surfaces. The oxygen vacancy in the reconstructed $(\sqrt{3} \times \sqrt{3})R30°$ surface introduces n-type character to the crystal, with an excess of electrons that will

distribute among other atoms. Similarly, the copper vacancies in the second model of the (111) surfaces introduce p-type character to the crystal, with an excess of positive charge that is distributed among the atoms. Table 1 shows the Bader charges of the four different (111) surfaces studied. The middle layer atoms of each slab exhibit bulklike charges, and the saturated oxygen atoms maintain a relatively consistent charge throughout the slabs. The coordinatively unsaturated surface copper atoms have much lower charges than the saturated copper atoms, with an average of $+0.37$ e for those originally unsaturated in the ideal and reconstructed surfaces (Cu_{CUS}). The surface copper and oxygen vacancies predominantly result in changes to the surface atom charges. The p-type character introduced by the copper vacancies in the (1×1)-V_{CuCUS} surface is exhibited as a delocalized decrease of the electron density in the oxygen and copper atoms of the first two layers of the slab. The n-type character introduced by the oxygen vacancy in the reconstructed surfaces results in a localized increase in electron density on the newly unsaturated surface copper atoms (Cu_{NN}), with charges of $+0.22$ and $+0.28$ e in the two reconstructed surfaces. The lower charges pinpoint excess electron density localized around the oxygen vacancy, which may play a significant role in affecting surface chemistry and adsorption for photocatalysis. In future work, it may therefore be important to model surface defects when studying the surface chemistry related to photocatalytic water splitting or conversion of carbon dioxide to methanol.

We calculate the energies associated with the (100), (110), and (111) surfaces according to eqs 6 and 7. While eq 6 can be applied to surfaces in a stoichiometric slab, such as the bulk-terminated (111) surface and the $(\sqrt{2} \times \sqrt{2})R45°$ (100) surface, eq 7 must be used to calculate the energies of surfaces in nonstoichiometric slabs. The nonstoichiometric slabs include the model for the O-terminated ideal (100) surface, which has an excess of oxygen because both surfaces of the slab must be O-terminated to retain inversion symmetry and prevent dipole formation. Models of the Cu-terminated (100) surface, both (110) surfaces, and the (111) surfaces with vacancies are similarly nonstoichiometric. Equation 7 requires that the two slabs used to calculate the averaged surface energy, scaled inversely by their individual surface areas, sum to a stoichiometric ratio of constituent atoms. For the (100) surface, this can be accomplished by using the O-terminated (1×1) and Cu-terminated $(3\sqrt{2} \times \sqrt{2})R45°$ surfaces as the two slabs. Similarly, the Cu- and Cu/O-terminated (110) surfaces can be used to calculate an averaged surface energy for the (110) surface. γ_{avg} of the (100) surface can be compared to the exact surface energy for the $(\sqrt{2} \times \sqrt{2})R45°$ surface to assess the accuracy of the averaged approaches. Unfortunately, there is no physically relevant complementary slab to the nonstoichiometric (111) surfaces that can be used to calculate an averaged surface energy according to eq 7, and so we do not calculate its surface energy within this method.

The surface energies, as calculated with eqs 6 and 7, are presented in Table 2. γ_{avg} of the (100) surface is within 0.3 J/m² of the exact surface energy for the $(\sqrt{2} \times \sqrt{2})R45°$, illustrating that the averaged approach gives some indication of the surface energy associated with a cleavage plane. However, the difference in the surface energies indicates that reconstruction and reorganization can significantly impact the surface energetics in addition to the simple choice of cleavage plane. The (111) surface energy is lower than the previous DFT-PBE-derived values of 0.71 and 0.76 J/m²,[18,40] as we have identified a

Table 2. Surface Energies (J/m²) of Cu₂O Surfaces, Calculated Using PBE+6

surface	surface energy (J/m²)
$(100) - (\sqrt{2} \times \sqrt{2})R45°$	1.171
$(100) - \gamma_{avg}$	1.471
$(110) - \gamma_{avg}$	1.171
$(111) - (1 \times 1)$	0.665

lower-energy surface that exhibits greater relaxation via breaking its bulklike symmetry. The (111) surface has the lowest surface energy, as expected of a nonpolar surface in comparison to the polar (100) and (110) surfaces.

Alternatively, we can calculate the free energies of each of the surfaces considered according to the method of ab initio atomistic thermodynamics, following eqs 14 and 17. These equations provide an upper bound and lower bound to the surface energies at low and high oxygen chemical potentials, with a linear dependence on the oxygen chemical potential between those two endpoints. Table 3 shows the calculated

Table 3. Surface Energies (J/m²) of Cu₂O Surfaces under O-Poor and O-Rich Conditions, Calculated Using PBE+6 and Ab Initio Atomistic Thermodynamics

	$\gamma_{O\text{-poor}}$ (J/m²)	$\gamma_{O\text{-rich}}$ (J/m²)
$(100) - (\sqrt{2} \times \sqrt{2})R45°$	1.171	1.171
$(100) - (1 \times 1)$	1.464	0.744
$(100) - (3\sqrt{2} \times \sqrt{2})R45°$	1.478	2.198
$(110) - $ Cu term.	1.586	2.096
$(110) - $ Cu/O term.	0.757	0.247
$(111) - (1 \times 1)$	0.665	0.665
$(111) - (\sqrt{3} \times \sqrt{3})R30°$	0.857	1.134
$(111) - (1 \times 1)$-V_{CuCUS}	0.599	0.183
$(111) - (\sqrt{3} \times \sqrt{3})R30°$-$V_{CuCUS}$	0.767	0.628

surface free energies at the two extrema, and Figure 4 plots the surface free energies as a function of oxygen chemical potential. Our surface free energies show a trend similar to that reported in ref 20, although our conclusions differ in that we identify the (1×1)-V_{CuCUS} surface as the most stable surface for all relevant
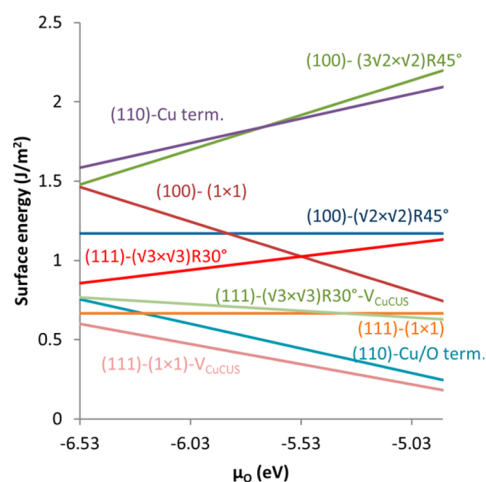

Figure 4. Surface free energies (J/m²) of Cu₂O surfaces as a function of oxygen chemical potential (eV). The oxygen chemical potential extends between the two bounds of O-poor (low chemical potential) and O-rich (higher chemical potential) environmental conditions.

chemical potentials, and we also predict that the stoichiometric (1×1) surface is more stable than the Cu/O-terminated (110) surface at low oxygen chemical potentials.

Figure 4 shows that the (1×1) (111) surfaces (with and without Cu_{CUS} atoms) are the most stable surfaces under oxygen-poor conditions. Therefore, we identify these as the predominant surfaces to be used for our band edge calculations. The Cu/O-terminated (110) is also relatively stable under most environmental conditions, according to our calculations. However, the (110) surface is rarely seen under common growth conditions.[42] Cu_2O microcrystals are typically either cubic or octahedral, indicating that the most stable faces are the {100} and {111} planes. In light of this conflict, we do not study the (110) surface for band edge calculations.

3.2. Cu_2O Band Edges. The first step in calculating the band edges of Cu_2O is determining the reference energy for the band structure. Figure 5 shows a schematic of how E_{BGC} or
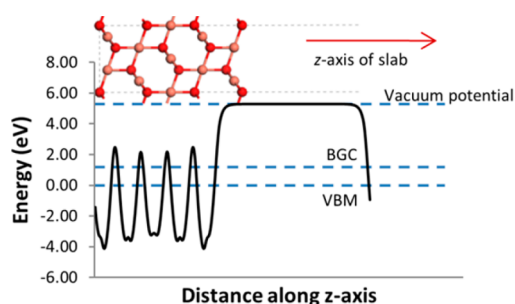

Figure 5. Averaged electrostatic potential along the z-axis for the Cu_2O(111) surface, calculated with PBE+U. Potentials of the vacuum region and for the band gap center are represented by the blue dashed lines. Energies are referenced to the Fermi level, which is defined here as the VBM.

E_{VBM} is referenced to E_{vac}, where the electrostatic potential is averaged over planes parallel to the surface to obtain the potential of the vacuum region. We first calculate the work function according to the standard method by referencing the VBM to the vacuum potential and approximating $E_f \approx E_{VBM}$, using PBE+U, DFT-HSE, and DFT-PBE0 (Table 4). The

Table 4. Energies of the VBM As Obtained by Directly Referencing the KS VBM to the Vacuum Potential (i.e., the Absolute Vacuum Energy Scale, or AVS)[a]

method	(1×1) E_{VBM} (eV)	(1×1)-V_{CuCUS} E_{VBM} (eV)
PBE+U	−5.29	−5.31
DFT-HSE	−5.62	−5.02
DFT-PBE0	−6.00	−5.97
Exp.		−5.25[b]

[a]Energies are calculated with PBE+U, DFT-HSE, and DFT-PBE0 and compared to the experimental value from in situ ECSTM (shifted to pH = 7). Energies are reported for both the (1×1) and (1×1)-V_{CuCUS} surfaces. Employing the approximation $E_f \approx E_{VBM}$, these values also represent $-\phi$. [b]Ref 2.

PBE0 functional leads to more strongly bound electrons and therefore increases the energy needed to extract an electron from the bulk crystal, resulting in the lowest energy for E_{VBM}. The energy difference between DFT-HSE and DFT-PBE0 is due to the long-range exact exchange expressed in PBE0 that is not included in the HSE functional. Long-range exact exchange may be appropriate in this case, as the extraction of an electron

from the crystal to the vacuum is a long-range process. In contrast, the PBE+U functional binds the electron the least, resulting in the highest E_{VBM}. While the value for E_{VBM} is sensitive to the functional used, all values are within 0.75 eV of the experimentally observed value of −5.25 eV (pH = 7), where the VBM was probed directly with in situ ECSTM. The experimental value was actually measured as −4.9 eV at a pH of 12.85, and we have shifted the energy to correspond to a pH of 7 according to[43]

$$E_{VBM}(pH_f) = E_{VBM}(pH_i) + 0.059(pH_f - pH_i) \quad (8)$$

Because our theoretical model is of a neutral surface, the pH shift should ideally be to the point of zero charge (pH_{pzc}) for a more accurate comparison of the experimental and theoretical energies. However, there are varying results for the values of pH_{pzc} due to its high sensitivity to experimental conditions,[44,45] and so without a known value for pH_{pzc}, we choose a pH of 7 as our neutral basis of comparison. The differing pH values may be a persistent contributor to the discrepancy between theory and experiment.

Because of the varying extent to which these functionals bind the electron to be extracted, the E_{VBM} derived directly from KS-DFT obeys the relation $E_{VBM}(PBE+U) > E_{VBM}(HSE) > E_{VBM}(PBE0)$. However, because of the increasing amounts of HF exchange in these functionals, their values for E_g exhibit the opposite trend, with $E_g(PBE+U) < E_g(HSE) < E_g(PBE0)$. As such, E_{BGC} should be expected to be less sensitive than the KS VBM to the choice of XC functional, as shown in earlier work by Toroker et al.[11] Table 5 shows the values for E_{BGC}

Table 5. Energies of the BGC (on the AVS), Calculated with PBE+U, DFT-HSE, and DFT-PBE0 for Both the (1×1) and (1×1)-V_{CuCUS} Surfaces

method	(1×1) E_{BGC} (eV)	(1×1)-V_{CuCUS} E_{BGC} (eV)
PBE+U	−4.67	−4.90
DFT-HSE	−4.67	−4.34
DFT-PBE0	−4.68	−4.63

referenced to the vacuum potential. As expected, there is negligible variation of E_{BGC} among the functionals for the (1×1) surface, validating it as a more reliable method than the earlier sole dependence on the KS VBM. This also shows that PBE+U can be used as a reliable and less computationally demanding alternative to hybrid functionals when deriving E_{BGC}. The greater variation for the (1×1)-V_{CuCUS} surface is likely due to the difficulty in defining the band edges in the slab, as the nonstoichiometry introduces p-type character that results in states at the Fermi level and different band edges for the different spin channels. This highlights the difficulty in using nonstoichiometric slabs when defining the band edges.

The band edges can then be subsequently determined using the band gap of 2.17 eV calculated from HSE + G_0W_0,[10] in combination with E_{BGC}, using eqs 4 and 5. The results, shown in Table 6, show agreement to experiment within 0.5 eV for the more consistent (1×1) surface. The differences between theory and experiment highlight the difficulty in obtaining accurate values for the pure, defect-free materials. Discrepancies may be due to theoretical approximations as well as defects in experimental samples (Cu_2O is known to be nonstoichiometric) and imperfect experimental measurements. Additionally, the differing pH between the experimental measurement and the theoretical model and the difficulty in properly framing

Table 6. E_{VBM} and E_{CBM} (on the AVS), Calculated by Using the Values for E_{BGC} from PBE+U, DFT-HSE, and DFT-PBE0 for Both the (1×1) and (1×1)-V_{CuCUS} Surfaces (Table 5) in Combination with the Fundamental Gap from HSE + G_0W_0[a]

| | E_{VBM} (eV) | | E_{CBM} (eV) | |
method	(1×1)	(1×1)-V_{CuCUS}	(1×1)	(1×1)-V_{CuCUS}
PBE+U	−5.75	−5.98	−3.58	−3.81
HSE	−5.75	−5.43	−3.58	−3.26
PBE0	−5.77	−5.71	−3.60	−3.54
Exp.	−5.25[b]		−3.15 ± 0.1[b]	

[a]Energies are compared to the experimental value from in situ ECSTM (shifted to pH = 7). [b]Refs 2 and 46.

their comparison with a known pH$_{pzc}$ will lead to an unaccounted-for shift of the band edge energies.

Finally, we compare the calculated band edges with the redox potentials for two reactions for which Cu$_2$O may be an ideal photocatalyst—water splitting and CO$_2$ conversion to methanol—whose potentials are given in Table 7. In principle, the

Table 7. Redox Potentials for the Half Reactions Involved in Water Splitting and Conversion of CO$_2$ to Methanol[a]

redox half-reaction	E (V, AVS)
$\frac{1}{2}O_2 + 2H^+ + 2e^- \rightleftharpoons H_2O$	5.26
$2H^+ + 2e^- \rightleftharpoons H_2$	4.03
$CO_2 + 6H^+ + 6e^- \rightleftharpoons CH_3OH + H_2O$	4.06

[a]Potentials are reported on the AVS and at pH = 7.

band edges should be compared to the redox free energies at pH$_{pzc}$, but due to the aforementioned difficulty of determining a single pH$_{pzc}$ for Cu$_2$O, we use pH = 7. While this introduces an additional approximation to our model, it is the best and most feasible approach at the moment. We use the band edges derived with the (1×1) surface, as there was a consistent prediction of the band edges with all DFT methods, showing the stoichiometric slab model's greater reliability. Figure 6 shows the relative positions of the band edges and the redox potentials. The potentials for the reduction of water and CO$_2$ lie below the CBM, while the oxidation potential of water lies above the VBM, indicating that photocatalytic water splitting or CO$_2$ conversion should be feasible on Cu$_2$O. This is in contrast
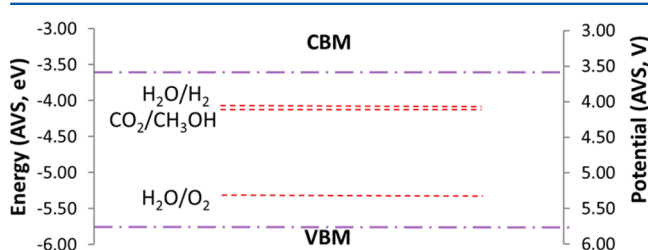

Figure 6. Theoretically derived Cu$_2$O band edges (purple dashed lines) in comparison to reaction redox potentials (red dashed lines) at pH = 7 and on the AVS. Energies for the redox reactions are calculated using a basis of one electron being transferred in the reaction. Theoretical band edge values correspond to the E_{BGC} value calculated with the (1×1) surface and the E_g value calculated with the HSE + G_0W_0 bulk calculation.

with the expectation of a small overpotential for the oxidation of water based on experimental measurements of the band edges.[1,47] However, our conclusions agree with other experimental evidence of photocatalytic water splitting on Cu$_2$O.[48] CO$_2$ conversion is being explored,[49−51] and our calculated band edges indicate that Cu$_2$O should be a viable photocatalyst in this application as well. As a caveat, note that these conclusions are based on a model of the surface with stoichiometric termination and no adsorbates, which therefore provides an ideal characterization of the material. Under experimental conditions, a further oxidized (or reduced) surface or surface adsorbates could shift the electrostatic potential and in turn the band edges to more unfavorable positions for these photocatalytic applications.

4. CONCLUSIONS

We have used PBE+U to characterize the surface structures of the low-index surfaces of Cu$_2$O for a number of terminations and reconstruction periodicities. For the (100) surface, we found that copper termination results in the formation of surface Cu−Cu dimers involving all surface copper cations, unrestricted from formation along the [011] direction. We observe that 1/2 O-termination does not prevent surface dimer formation, in contrast with the interpretation of earlier measurements offered by experimentalists. Complete O-termination of the (100) surface results in smaller surface relaxations. For the (110) surface, we showed that regardless of termination the outermost surface relaxes inward toward the bulk. The bulk-terminated (1×1) (111) surface relaxes to a structure with broken symmetry to form a surface copper dimer, whereas the (1×1) (111) surface with copper vacancies relaxes negligibly. Finally, the reconstructed $(\sqrt{3} \times \sqrt{3})$R30° (111) surfaces (both with and without surface copper vacancies) form clusters of copper atoms around the surface oxygen vacancy. These copper clusters are characterized by greater localized electron density, which may have a significant impact on the surface chemistry of the (111) surface.

The (1×1) (111) surfaces were identified as lowest in energy and were used for calculation of the band edges. We showed the sensitivity of E_{VBM} to the XC functional when directly referencing the KS VBM to the vacuum energy. This sensitivity was reduced when using the formally exact method of setting the BGC as a reference, validating this approach for calculating the band edges, consistent with earlier work by Toroker et al.[11] The stoichiometric slab showed greater consistency in its band edge prediction, illustrating the difficulty in using nonstoichiometric slabs when defining band edges. This consistency indicates that PBE+U could be used as a less expensive alternative to hybrid functionals when deriving the band edges, provided that HSE/G_0W_0 is still used to define the band gap. Comparison of the band edges to redox potentials revealed that Cu$_2$O is a promising photocatalyst for water splitting and CO$_2$ conversion to methanol.

■ AUTHOR INFORMATION

Corresponding Author
*Phone: 609-258-5391. Fax: 609-258-5877. E-mail: eac@princeton.edu.

Notes

The authors declare no competing financial interest.

■ ACKNOWLEDGMENTS

■ REFERENCES

(1) Schöppel, H. R.; Gerischer, H. Die kathodische Reduktion von Cu-I-oxid-Elektroden als Beispiel für den Mechanismus der Reduktion eines Halbleiter-Kristalls. *Ber. Bunsenges. Phys. Chem.* **1971**, *75*, 1237−1239.

(2) Caballero-Briones, F.; Artés, J. M.; Díez-Pérez, I.; Gorostiza, P.; Sanz, F. Direct Observation of the Valence Band Edge by in Situ ECSTM-ECTS in p-Type Cu$_2$O Layers Prepared by Copper Anodization. *J. Phys. Chem. C* **2009**, *113*, 1028−1036.

(3) Janak, J. F. Proof that $\partial E/\partial n_i = \varepsilon$ in Density-Functional Theory. *Phys. Rev. B* **1978**, *18*, 7165−7168.

(4) Xiang, H.; Wei, S.-H.; Gong, X. Identifying Optimal Inorganic Nanomaterials for Hybrid Solar Cells. *J. Phys. Chem. C* **2009**, *113*, 18968−18972.

(5) Rutter, M. J.; Robertson, J. Ab Initio Calculation of Electron Affinities of Diamond Surfaces. *Phys. Rev. B* **1998**, *57*, 9241−9245.

(6) Vogtenhuber, D.; Podloucky, R.; Neckel, A.; Steinemann, S. G.; Freeman, A. J. Electronic Structure and Relaxed Geometry of the TiO$_2$ Rutile (110) Surface. *Phys. Rev. B* **1994**, *49*, 2099−2103.

(7) Liu, W.; Zheng, W. T.; Jiang, Q. First-principles Study of the Surface Energy and Work Function of III-V Semiconductor Compounds. *Phys. Rev. B* **2007**, *75*, 235322−1−8.

(8) Perdew, J. P.; Levy, M. Physical Content of the Exact Kohn-Sham Orbital Energies: Band Gaps and Derivative Discontinuities. *Phys. Rev. Lett.* **1983**, *51*, 1884−1887.

(9) Teale, A. M.; De Proft, F.; Tozer, D. J. Orbital Energies and Negative Electron Affinities from Density Functional Theory: Insight from the Integer Discontinuity. *J. Chem. Phys.* **2008**, *129*, 044110−1−12.

(10) Isseroff, L. Y.; Carter, E. A. Importance of Reference Hamiltonians Containing Exact Exchange for Accurate One-Shot GW Calculations of Cu$_2$O. *Phys. Rev. B* **2012**, *85*, 235142−1−7.

(11) Toroker, M. C.; Kanan, D. K.; Alidoust, N.; Isseroff, L. Y.; Liao, P.; Carter, E. A. First Principles Scheme to Evaluate Band Edge Positions in Potential Transition Metal Oxide Photocatalysts and Photoelectrodes. *Phys. Chem. Chem. Phys.* **2011**, *13*, 16644−16654.

(12) Höffling, B.; Schleife, A.; Fuchs, F.; Rödl, C.; Bechstedt, F. Band Lineup Between Silicon and Transparent Conducting Oxides. *Appl. Phys. Lett.* **2010**, *97*, 032116−1−−3.

(13) Faleev, S. V.; Mryasov, O. N.; Mattsson, T. R. Quasiparticle Self-Consistent GW Calculation of the Work Functions of Al(111), Al(100), and Al(110). *Phys. Rev. B* **2010**, *81*, 205436−1−−7.

(14) Schulz, K. H.; Cox, D. F. Photoemission and Low-Energy-Electron-Diffraction Study of Clean and Oxygen-Dosed Cu$_2$O (111) and (100) Surfaces. *Phys. Rev. B* **1991**, *43*, 1610−1621.

(15) Önsten, A.; Göthelid, M.; Karlsson, U. O. Atomic structure of Cu$_2$O(1 1 1). *Surf. Sci.* **2009**, *603*, 257−264.

(16) McClenaghan, N. A Density Functional Theory Study of the Surface Relaxation and Reactivity of Cu$_2$O(100). *Surf. Sci.* **2000**, *464*, 223−232.

(17) Le, D.; Stolbov, S.; Rahman, T. S. Reactivity of the Cu$_2$O(1 0 0) Surface: Insights from First Principles Calculations. *Surf. Sci.* **2009**, *603*, 1637−1645.

(18) Islam, M. M.; Diawara, B.; Maurice, V.; Marcus, P. Bulk and Surface Properties of Cu$_2$O: A First-Principles Investigation. *J. Mol. Struct. THEOCHEM* **2009**, *903*, 41−48.

(19) Soon, A.; Todorova, M.; Delley, B.; Stampfl, C. Thermodynamic Stability and Structure of Copper Oxide Surfaces: A First-Principles Investigation. *Phys. Rev. B* **2007**, *75*, 125420−1−9.

(20) Soon, A.; Todorova, M.; Delley, B.; Stampfl, C. Erratum: Thermodynamic Stability and Structure of Copper Oxide Surfaces: A First-Principles Investigation [Phys. Rev. B 75, 125420 (2007)]. *Phys. Rev. B* **2007**, *76*, 129902−1.

(21) Perdew, J. P.; Burke, K.; Ernzerhof, M. Generalized Gradient Approximation Made Simple. *Phys. Rev. Lett.* **1996**, *77*, 3865−3868.

(22) Perdew, J. P.; Burke, K.; Ernzerhof, M. Generalized Gradient Approximation Made Simple [Phys. Rev. Lett. 77, 3865 (1996)]. *Phys. Rev. Lett.* **1997**, *78*, 1396−1396.

(23) Anisimov, V. I.; Zaanen, J.; Andersen, O. K. Band theory and Mott insulators: Hubbard U instead of Stoner I. *Phys. Rev. B* **1991**, *44*, 943−954.

(24) Dudarev, S. L.; Liechtenstein, A. I.; Castell, M. R.; Briggs, G. A. D.; Sutton, A. P. Surface States on NiO (100) and the Origin of the Contrast Reversal in Atomically Resolved Scanning Tunneling Microscope Images. *Phys. Rev. B* **1997**, *56*, 4900−4908.

(25) Heyd, J.; Scuseria, G. E.; Ernzerhof, M. Hybrid Functionals Based on a Screened Coulomb Potential. *J. Chem. Phys.* **2003**, *118*, 8207−8215.

(26) Heyd, J.; Scuseria, G. E. Assessment and Validation of a Screened Coulomb Hybrid Density Functional. *J. Chem. Phys.* **2004**, *120*, 7274−7280.

(27) Heyd, J.; Scuseria, G. E. Efficient Hybrid Density Functional Calculations in Solids: Assessment of the Heyd−Scuseria−Ernzerhof Screened Coulomb Hybrid Functional. *J. Chem. Phys.* **2004**, *121*, 1187−1192.

(28) Reuter, K.; Scheffler, M. Composition, Structure, and Stability of RuO$_2$(110) as a Function of Oxygen Pressure. *Phys. Rev. B* **2001**, *65*, 035406−1−11.

(29) Reuter, K.; Scheffler, M. First-Principles Atomistic Thermodynamics for Oxidation Catalysis: Surface Phase Diagrams and Catalytically Interesting Regions. *Phys. Rev. Lett.* **2003**, *90*, 046103-1−4.

(30) Straumanis, M. E.; Yu, L. S. Lattice Parameters, Densities, Expansion Coefficients and Perfection of Structure of Cu and of Cu−In α Phase. *Acta Crystallogr. Sect.* **1969**, *25*, 676−682.

(31) Lide, D. R. *CRC Handbook of Chemistry and Physics 2012−2013*; CRC Press: Boca Raton, FL, 2012.

(32) Kresse, G.; Joubert, D. From Ultrasoft Pseudopotentials to the Projector Augmented-Wave Method. *Phys. Rev. B* **1999**, *59*, 1758−1775.

(33) Blöchl, P. E. Projector Augmented-Wave Method. *Phys. Rev. B* **1994**, *50*, 17953−17979.

(34) Dudarev, S. L.; Botton, G. A.; Savrasov, S. Y.; Humphreys, C. J.; Sutton, A. P. Electron-Energy-Loss Spectra and the Structural Stability of Nickel Oxide: An LSDA+U Study. *Phys. Rev. B* **1998**, *57*, 1505−1509.

(35) Blöchl, P. E.; Jepsen, O.; Andersen, O. K. Improved Tetrahedron Method for Brillouin-Zone Integrations. *Phys. Rev. B* **1994**, *49*, 16223−16233.

(36) Adamo, C.; Barone, V. Toward Reliable Density Functional Methods Without Adjustable Parameters: The PBE0 Model. *J. Chem. Phys.* **1999**, *110*, 6158−6170.

(37) Krukau, A. V.; Vydrov, O. A.; Izmaylov, A. F.; Scuseria, G. E. Influence of the Exchange Screening Parameter on the Performance of Screened Hybrid Functionals. *J. Chem. Phys.* **2006**, *125*, 224106−1−5.

(38) Kresse, G.; Bergermayer, W.; Podloucky, R.; Lundgren, E.; Koller, R.; Schmid, M.; Varga, P. Complex Surface Reconstructions Solved by Ab Initio Molecular Dynamics. *Appl. Phys.* **2003**, *76*, 701−710.

(39) Islam, M. M.; Diawara, B.; Maurice, V.; Marcus, P. Surface Reconstruction Modes of Cu$_2$O(001) Surface: A First Principles Study. *Surf. Sci.* **2010**, *604*, 1516−1523.

(40) Soon, A.; Sohnel, T.; Idriss, H. Plane-Wave Pseudopotential Density Functional Theory Periodic Slab Calculations of CO Adsorption on Cu$_2$O(111) Surface. *Surf. Sci.* **2005**, *579*, 131−140.

(41) Tang, W.; Sanville, E.; Henkelman, G. A grid-based Bader analysis algorithm without lattice bias. *J. Phys.: Condens. Matter* **2009**, *21*, 084204−084204−7.

(42) Siegfried, M. J.; Choi, K.-S. Elucidating the Effect of Additives on the Growth and Stability of Cu_2O Surfaces via Shape Transformation of Pre-Grown Crystals. *J. Am. Chem. Soc.* **2006**, *128*, 10356−10357.

(43) Bolts, J. M.; Wrighton, M. S. Correlation of Photocurrent-Voltage Curves with Flat-Band Potential for Stable Photoelectrodes for the Photoelectrolysis of Water. *J. Phys. Chem.* **1976**, *80*, 2641−2645.

(44) Kosmulski, M. *Surface Charging and Points of Zero Charge*; CRC Press: Boca Raton, FL, 2009.

(45) Matijević, E.; Bell, A.; Brace, R.; McFadyen, P. Formation and Surface Characteristics of Hydrous Metal Oxide Sols. *J. Electrochem. Soc.* **1973**, *120*, 893−899.

(46) Brahms, S.; Nikitine, S.; Dahl, J. P. On the Band Structure and the Absorption Spectrum of Cu_2O. *Phys. Lett.* **1966**, *22*, 31−33.

(47) Jongh, P. E.; de Vanmaekelbergh, D.; Kelly, J. J. Cu_2O: A Catalyst for the Photochemical Decomposition of Water? *Chem. Commun.* **1999**, 1069−1070.

(48) Hara, M.; Kondo, T.; Komoda, M.; Ikeda, S.; Kondo, J. N.; Domen, K.; Hara, M.; Shinohara, K.; Tanaka, A. Cu_2O as a Photocatalyst for Overall Water Splitting Under Visible Light Irradiation. *Chem. Commun.* **1998**, 357−358.

(49) Frese, J. Electrochemical Reduction of CO_2 at Intentionally Oxidized Copper Electrodes. *J. Electrochem. Soc.* **1991**, *138*, 3338−3344.

(50) Le, M.; Ren, M.; Zhang, Z.; Sprunger, P. T.; Kurtz, R. L.; Flake, J. C. Electrochemical Reduction of CO_2 to CH_3OH at Copper Oxide Surfaces. *J. Electrochem. Soc.* **2011**, *158*, E45−E49.

(51) Ghadimkhani, G.; Tacconi, N. R.; de Chanmanee, W.; Janaky, C.; Rajeshwar, K. Efficient Solar Photoelectrosynthesis of Methanol from Carbon Dioxide Using Hybrid $CuO−Cu_2O$ Semiconductor Nanorod Arrays. *Chem. Commun.* **2013**, *49*, 1297−1299.